HHS Public Access

Author manuscript

Opt Lett. Author manuscript; available in PMC 2019 October 15.

Published in final edited form as:

Opt Lett. 2018 October 15; 43(20): 4875–4878. doi:10.1364/OL.43.004875.

Dual-view photoacoustic microscopy for quantitative cell nuclear imaging

De Cai[#1,2], **Terence T. W. Wong**[#1,3], **Liren Zhu**[1], **Junhui Shi**[1], **Sung-Liang Chen**[2], and **Lihong V. Wang**[1,*]

[1]Caltech Optical Imaging Laboratory, Andrew and Peggy Cherng Department of Medical Engineering, Department of Electrical Engineering, California Institute of Technology, Pasadena, California 91125, USA

[2]University of Michigan-Shanghai Jiao Tong University Joint Institute, Shanghai Jiao Tong University, Shanghai 200240, China

[3]Present address: Translational and Advanced Bioimaging Laboratory, Department of Chemical and Biological Engineering, Hong Kong University of Science and Technology, Hong Kong, China

[#] These authors contributed equally to this work.

Abstract

Optical-resolution photoacoustic microscopy (OR-PAM) is an emerging imaging modality for studying biological tissues. However, in conventional single-view OR-PAM, the lateral and axial resolutions—determined optically and acoustically, respectively—are highly anisotropic. In this Letter, we introduce dual-view OR-PAM (DV-OR-PAM) to improve the axial resolution, achieving three-dimensional (3D) resolution isotropy. We first use 0.5 μm polystyrene beads and carbon fibers to validate the resolution isotropy improvement. Imaging of mouse brain slices further demonstrates the improved resolution isotropy, revealing the 3D structure of cell nuclei in detail, which facilitates quantitative cell nuclear analysis.

Keywords

(110.0180) Microscopy; (110.5120) Photoacoustic imaging; (170.3880) Medical and biological imaging; (100.6890) Three-dimensional image processing

Optical-resolution photoacoustic microscopy (OR-PAM) has found broad applications in imaging biological objects ranging from organelles to organs [1, 2]. OR-PAM can achieve lateral resolution in several micrometers or even sub-micrometers [3, 4] by tightly focusing the optical focal spot. However, the axial resolution in ORPAM, which is determined by the bandwidth of an ultrasonic transducer matching the targeted tissue penetration, is typically limited to tens of micrometers. The anisotropic resolutions hindered OR-PAM from revealing accurate three-dimensional (3D) structures of biological tissue.

[*]Corresponding author: LVW@Caltech.edu.

OR-PAM with ultraviolet laser illumination has recently been exploited to image human breast and mouse brain tissues with specific cell nuclear contrast for cancer diagnosis and intraoperative margin assessment as well as for basic research in neuroscience [5–8]. The resolution anisotropy in OR-PAM with ultraviolet laser illumination is particularly severe due to the finer optical lateral resolution enabled by the shorter laser wavelength (e.g., 0.33 μm lateral resolution versus 48 μm axial resolution [5]).

In recent years, different approaches have been developed to enhance the axial resolution, thus improving the resolution isotropy of OR-PAM. Wide bandwidth ultrasonic transducers [9] and optical ultrasonic detectors [10] have been utilized for high-frequency ultrasonic detection to refine axial resolution, yet the severe attenuation of high-frequency acoustic waves in biological tissue limits the imaging depth and working distance. Although the Weiner deconvolution algorithm has also been utilized to improve the axial resolution, the improvement is not significant due to the stringent signal-noise ratio (SNR) requirement [11]. Moreover, optical sectioning has been achieved in OR-PAM by nonlinear effects such as two-photon absorption [12] and Grüneisen relaxation [13, 14]; the imaging speed, however, is reduced owing to the need for additional depth scanning. Multi-view optical illumination has been applied in both light sheet fluorescence microscopy [15, 16] and OR-PAM [17, 18], to improve the resolution isotropy. In particular, in the previous demonstration of multi-view OR-PAM [17], the sample was required to be rotated to achieve multi-view optical illumination, which may introduce undesirable movement of the sample. Furthermore, the previous work [17, 19] proved that dual-view is sufficient in providing isotropic resolution on the condition that a complementary, perpendicular view is acquired and properly merged.

In this Letter, we report dual-view OR-PAM (DV-OR-PAM) with ultraviolet laser illumination, developed to improve resolution isotropy. The schematic of DV-OR-PAM is illustrated in Fig. 1. The 5-mm-diameter UV laser beam (Wedge-HF-266, 266-nm wavelength, Bright Solutions SRL) is split into two orthogonal beams, named as the left and right view laser beams hereafter. The two beams are then focused onto the sample from below, each by an aspheric lens with an NA of 0.29 (AFL25–40-S-U, asphericon GmbH). The ultrasonic waves generated inside the sample through the photoacoustic effect are detected by an ultrasonic transducer (V358-SU, 50-MHz central frequency, 88% bandwidth (one-way), Olympus NDT, Inc.) with a homemade concave lens at the front to provide acoustic focusing. After electrical amplification (56 dB, two ZFL-500LN+, Mini-Circuits, Inc.), the signal is digitized by a data acquisition card (ATS9350, Alazar Technologies, Inc.) at a sampling rate of 500 MS/s and sent to a computer for afterward processing. Each A-line signal is converted to a depth-resolved profile by taking the envelope. The water tank with the sample is raster scanned with a step size of 0.31 μm on the *x*-*y* plane by a motorized scanning stage (PLS-85, PI miCos GmbH) to obtain a single-view 3D image (e.g., the left view). The sample is then re-scanned with the same configuration but with the right view laser beam to obtain an orthogonal-view 3D image.

The axial pixel size in the original 3D images is 3 μm (assuming the speed of sound is 1.5 mm/μs), which is larger than the lateral pixel size (0.31 μm). Interpolation is applied in the axial direction to make the pixel size isotropic. The optical axes of the dual-view beams,

together with the detection axis of the ultrasonic transducer, are coplanar on the *x-z* plane and symmetrically aligned with respect to the ultrasonic transducer axis, both with 45-degree tilt angles. The left and right view images are transformed to a coordinate system of the sample for image registration through an affine transformation, including both shear and translation transformations, as shown in Eq. 1, where *x', y'* and *z'* are the coordinates in the sample system; *x, y,* and z are the local coordinates for the two views; t_x, t_y and t_z constitute the translation vector for the transformation matrix. The shear transformation is performed on the *x-z* plane. The x coordinate transformations for the left and right view images are $x' = x - z$ and $x' = x + z$, respectively. The effect of the shear transformation is illustrated in Figs. 1(b) and 1(c) for the left and right view images, respectively.

$$\begin{bmatrix} x' \\ y' \\ z' \\ 1 \end{bmatrix} = \begin{bmatrix} 1 & 0 & \pm 1 & t_x \\ 0 & 1 & 0 & t_y \\ 0 & 0 & 1 & t_z \\ 0 & 0 & 0 & 1 \end{bmatrix} \begin{bmatrix} x \\ y \\ z \\ 1 \end{bmatrix} \quad (1)$$

Sub-resolution polystyrene beads with a 0.5 μm average diameter, together with a target to be imaged, were embedded in agarose gel as registration markers [20]. The beads were detected in the two view images and localized as point objects for registration. Values of t_x, t_y and t_z in Eq. 1 are optimized by globally minimizing the total displacement between the corresponding registration point objects between the left and right view images.

The sub-resolution beads were also used to extract the point spread functions (PSFs) in the two view images. The single bead images were averaged over four acquisitions, and normalized to serve as the PSFs of the two view images. The PSFs were also affine transformed accordingly to co-register. The co-registered two view images and PSFs were then used for dual-view Richardson-Lucy deconvolution with 10 iterations [16, 20] to obtain a single dual-view image.

We used the sub-resolution beads to calibrate the resolutions of the original two images and the dual-view image. The volumetrically rendered 3D images of a single bead are shown in Figs. 2(a), 2(b), and 2(c) for the left view, the right view, and the dual view, respectively. Note that the original left and right view images were not affine transformed. The resolutions defined by the full width at half maximum are plotted in Fig. 2(d). The resolutions on the *x*-axis are 3.0 μm, 2.6 μm, and 1.8 μm for the left view, the right view, and the dual view, respectively. The resolutions on the *y*-axis are 1.7 μm, 1.7 μm and 1.3 μm for the left view, the right view, and the dual view, respectively. The acoustically determined axial resolution of the original left and right view images, far worse than the optically defined lateral resolutions, is 37 μm, which account for the elongated bead profiles and resolution anisotropy (Figs. 2(a), 2(b)). Dual-view imaging greatly improved the axial resolution to 1.8 μm (i.e., by a factor of 20), making the bead profile nearly isotropic in 3D (blue bars in Fig. 2(d)). As the dual-view deconvolution is performed on the *x-z* plane, the *x-z* resolution isotropy—quantified as the ratio between the *x* and *z* resolution—is improved

from 12.3/14.2 (left view/right view) to 1.0. The resolutions in the original two views in the *x* direction are about $\sqrt{2}$ larger than the resolutions in the *y* direction because of the oblique 45-degree illumination with respect to the *z*-axis. The resolution on the y-axis for oblique illumination is the same as normal incident illumination. In addition, the *x* and *y* resolutions are improved in the dual-view images due to deconvolution in the reconstruction algorithm.

To better demonstrate the performance of DV-OR-PAM, we made a 3D tissue phantom composed of 6-μm-diameter carbon fibers placed at different depths and orientations. The 3D images of the carbon fibers are shown in Figs. 3(a), 3(b), and 3(c) for the left view, the right view, and the dual view, respectively. A clearer carbon fiber network is revealed in the dual-view image due to the enhanced axial resolution and ~9 dB SNR improvement. The improved resolution isotropy in DV-OR-PAM can reveal finer depth information as shown in Figs. 3(d), 3(e), and 3(f), which are the *y*-*z* maximum amplitude projections (MAP) of the volumetric images shown in Figs. 3(a), 3(b), and 3(c). The carbon fibers at different depths are clearly revealed in the dual-view *y*-*z* MAP image, while in the original two *y*-*z* MAP images, the two carbon fibers are unresolved due to the poor axial resolution.

We imaged mouse brain slices of 200 μm thickness [6] to further validate DV-OR-PAM. To enlarge the imaging area, the step size was set as 0.62 μm with an imaging field of view over 1 mm × 0.5 mm along the *x* and *y* axes. The absorption contrast at the 266 nm wavelength in mouse brains is predominantly cell nuclei [8], which appear to be the brightest features in the images. The *x*-*y* MAP images of the mouse brain slice are shown in Figs. 4(a), 4(b), and 4(c) for the left view, the right view, and the dual view, respectively. To better visualize the improved image quality of DVOR-PAM, zoomed-in images of the red dashed boxes are shown in Figs. 4(d), 4(e), and 4(f). The cell nuclei can be better identified in the dual-view image with improvement in both resolution and SNR (by ~10 dB). Specifically, the cell nuclear profile in the blue dashed boxes, which cannot be resolved in the original two images (Figs. 4(g) and 4(h)), can be clearly revealed in the dual-view image as shown in Fig. 4(i). The detailed internal structure of the cell nuclei provided by DV-OR-PAM can potentially facilitate accurate cancer diagnosis [21, 22].

We have digitally extracted the image stacks on the *x*-*y* plane of the red dashed regions at five different depths with an interval of 3.1 μm. The image stacks are shown in Figs. 4(j)-(l) for the left view, right view, and dual view images, respectively. In the original images, the image stacks at five different depths show a similar brightness because of the poor axial resolution, while in the dual-view image, different layers of cell nuclei are clearly demonstrated.

With the improved axial resolution, it is possible to reveal the accurate 3D shape of a cell nucleus as shown in Figs. 5(a)-(c), corresponding to the red dashed regions shown in Figs. 4(a)-(c). We quantitatively analyzed the cell nuclear volume, with a histogram plotted in Fig. 5(d). The average cell nuclear volumes are 5312 ± 2202 μm^3 and 6665 ± 2253 μm^3 for the left and right views, respectively. While in the dual-view image, the average cell nuclear volume is 778 ± 396 μm^3, which is much closer to the realistic cell nuclear volume if an average diameter of 6 μm and a spherical shape are assumed [23]. Cell nuclear volumes and shapes are important diagnostic features for cancer diagnosis [24].

In conclusion, a dual-view optical illumination for axial resolution improvement in OR-PAM was developed. Sub-resolution beads and carbon fiber phantoms were used to validate the axial resolution improvement and resolution isotropy. The SNR of the dual-view images was also improved. We used mouse brain slices to further demonstrate the efficacy of DV-OR-PAM for quantitative cell nuclear analysis. The DV-OR-PAM is a promising tool for cancer diagnosis by providing quantitative 3D cell nuclear information.

Acknowledgments.

D. Cai appreciates the support from China Scholarship Council. L. V. Wang has a financial interest in Microphotoacoustics, Inc., CalPACT, LLC, and Union Photoacoustic Technologies, Ltd., which, however, did not support this work.

Funding.

This work was sponsored by National Institutes of Health (NIH) Grants DP1 EB016986 (NIH Director's Pioneer Award), R01 CA186567 (NIH Director's Transformative Research Award), U01 NS090579 (NIH BRAIN Initiative), and U01 NS099717 (NIH BRAIN Initiative).

References

1. Wang LV, and Yao J, Nat. Methods 13, 627(2016). [PubMed: 27467726]
2. Wang LV, and Hu S, Science 335, 1458–1462 (2012). [PubMed: 22442475]
3. Zhang C, Maslov KI, Hu S, Wang LV, Chen R, Zhou Q, and Shung KK, J. Biomed. Opt 17, 020501(2012). [PubMed: 22463018]
4. Hu S, Maslov K, and Wang LV, Opt. Lett 36, 1134–1136 (2011). [PubMed: 21479007]
5. Wong TT, Zhang R, Hai P, Zhang C, Pleitez MA, Aft RL, Novack DV, and Wang LV, Sci. Adv 3, e1602168(2017). [PubMed: 28560329]
6. Wong TT, Zhang R, Zhang C, Hsu H-C, Maslov KI, Wang L, Shi J, Chen R, Shung KK, and Zhou Q, Nat. Commun 8, 1386(2017). [PubMed: 29123109]
7. Yao D, Chen R, Maslov K, Zhou Q, and Wang LV, J. Biomed. Opt 17, 056004–056004 (2012). [PubMed: 22612127]
8. Yao D-K, Maslov K, Shung KK, Zhou Q, and Wang LV, Opt. Lett 35, 4139–4141 (2010). [PubMed: 21165116]
9. Strohm EM, Berndl ES, and Kolios MC, Photoacoustics 1, 49–53 (2013). [PubMed: 25302149]
10. Xie Z, Chen S-L, Ling T, Guo LJ, Carson PL, and Wang X, Opt. Express 19, 9027–9034 (2011). [PubMed: 21643156]
11. Zhang C, Maslov KI, Yao J, and Wang LV, J. Biomed. Opt 17, 116016(2012). [PubMed: 23123975]
12. Yamaoka Y, Nambu M, and Takamatsu T, Opt. Express 19, 13365–13377 (2011). [PubMed: 21747492]
13. Liu X, Wong TT, Shi J, Ma J, Yang Q, and Wang LV, Opt. Lett 43, 947–950 (2018). [PubMed: 29444034]
14. Wang L, Zhang C, and Wang LV, Phys. Rev. Lett 113, 174301(2014). [PubMed: 25379919]
15. Wu Y, Chandris P, Winter PW, Kim EY, Jaumouillé V, Kumar A, Guo M, Leung JM, Smith C, and Rey-Suarez I, Optica 3, 897–910 (2016). [PubMed: 27761486]
16. Preibisch S, Amat F, Stamataki E, Sarov M, Singer RH, Myers E, and Tomancak P, Nat. Methods 11, 645(2014). [PubMed: 24747812]
17. Zhu L, Li L, Gao L, and Wang LV, Optica 1, 217–222 (2014). [PubMed: 25558469]
18. Zhu L, Gao L, Li L, Wang L, Ma T, Zhou Q, Shung KK, and Wang LV, "Cross-optical-beam nonlinear photoacoustic microscopy," in Photons Plus Ultrasound: Imaging and Sensing 2014 (International Society for Optics and Photonics2014), p. 89433H.

19. Wu Y, Wawrzusin P, Senseney J, Fischer RS, Christensen R, Santella A, York AG, Winter PW, Waterman CM, and Bao Z, Nat. Biotechnol 31, 1032(2013). [PubMed: 24108093]
20. Preibisch S, Saalfeld S, Schindelin J, and Tomancak P, Nat. Methods 7, 418(2010). [PubMed: 20508634]
21. Backman V, Wallace MB, Perelman L, Arendt J, Gurjar R, Müller M, Zhang Q, Zonios G, Kline E, and McGillican T, Nature 406, 35(2000). [PubMed: 10894529]
22. Vona G, Sabile A, Louha M, Sitruk V, Romana S, Schütze K, Capron F, Franco D, Pazzagli M, and Vekemans M, Am. J. Pathol 156, 57–63 (2000). [PubMed: 10623654]
23. Bernhard W, and Granboulan N, Exp. Cell. Res 9, 19–53 (1963).
24. Zink D, Fischer AH, and Nickerson JA, Nat. Rev. Cancer 4, 677(2004). [PubMed: 15343274]

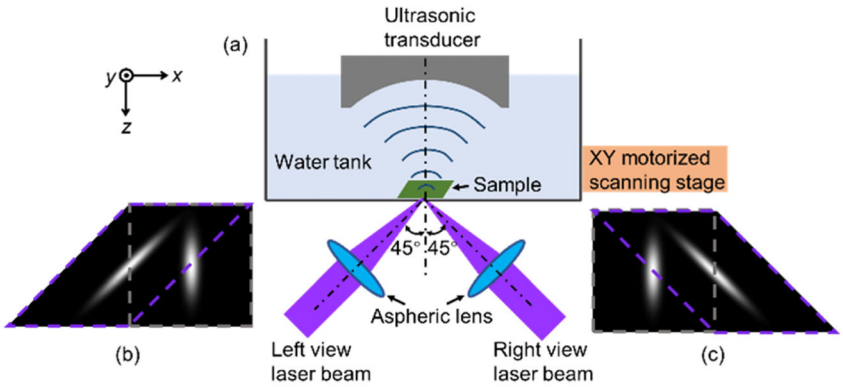

Fig. 1.

(a) Schematic of the DV-OR-PAM system. (b), (c) Shear transformed images in the purple dashed boxes for the left and right views, respectively. The corresponding original images are enclosed in the gray dashed boxes for comparison.

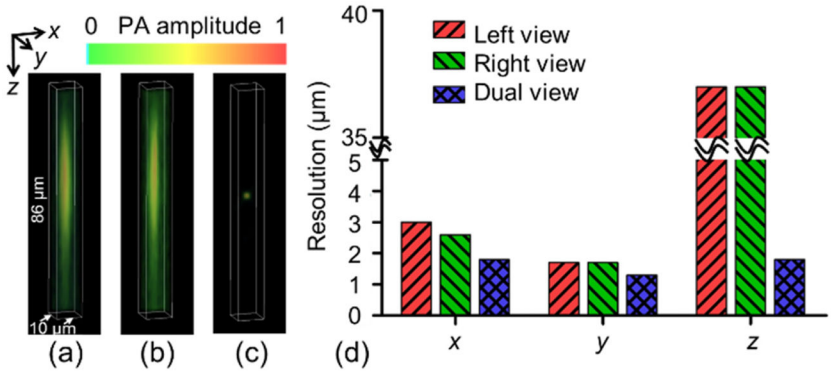

Fig. 2.

Resolution calibration for DV-OR-PAM using 0.5-μm-diameter beads as point objects. Volumetrically rendered bead images for (a) the left view, (b) the right view, and (c) the dual view, respectively. (d) Resolutions in the *x, y,* and *z* directions for the left view, the right view, and the dual view images.

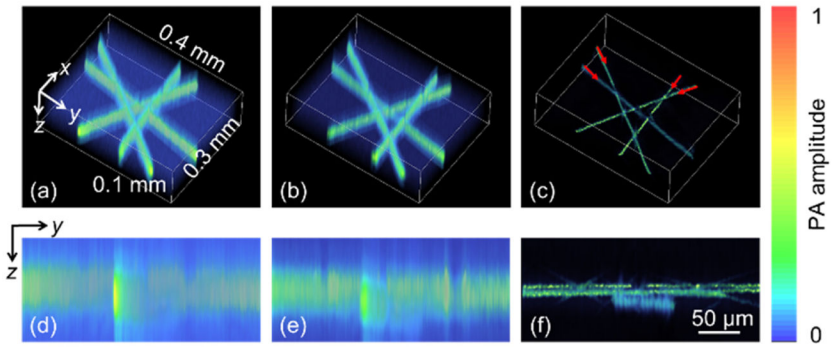

Fig. 3.

Imaging of four 6-μm-diameter carbon fibers (indicated by red arrows) with different depths and orientations. Volumetric carbon fiber images for (a) the left view, (b) the right view, and (c) the dual view. *y*-*z* MAP images to show the depth information for (d) the left view, (e) the right view, and (f) the dual view.

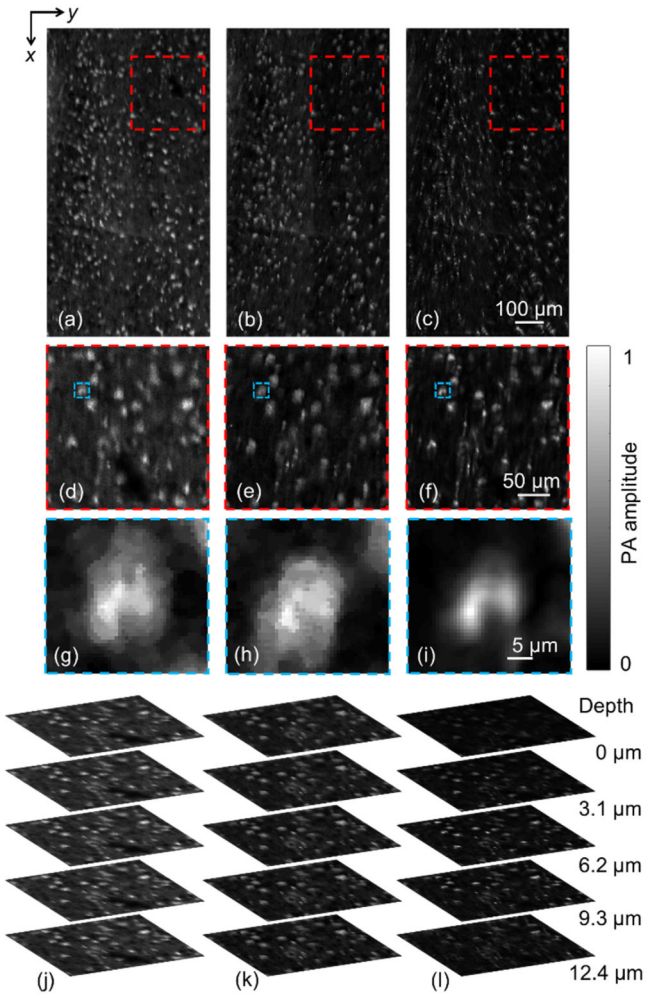

Fig. 4.

Imaging of a mouse brain slice. *x-y* MAP images for (a) the left view, (b) the right view, and (c) the dual view, respectively. (d)-(f) Zoomed-in red dashed regions of (a)-(c). (g)-(i) Zoomed-in blue dashed regions of (d)-(f), showing the cell nuclear profile. Digitally reconstructed *x-y* images of the red dashed regions at five different depths with an interval of 3.1 μm for (j) the left view, (k) the right view, and (l) the dual view, respectively.

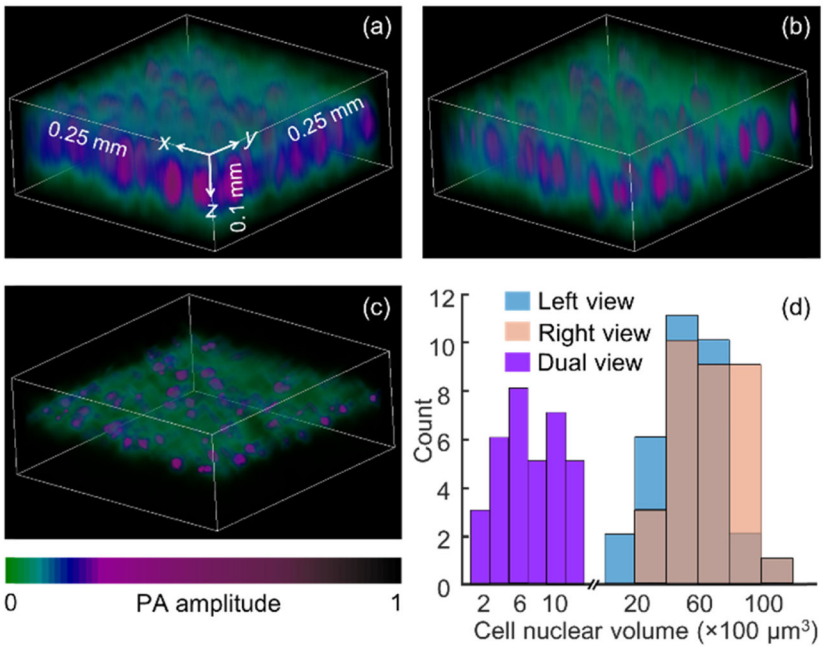

Fig. 5.

Volumetric rendering of mouse brain slice images corresponding to the red dashed regions in Fig. 4 for (a) the left view, (b) the right view, and (c) the dual view. (d) Histogram of the cell nuclear volumes imaged by the original two views and the dual view.